Cholesterol-Dependent Nanomechanical Stability of Phase-Segregated Multicomponent Lipid Bilayers

Ruby May A. Sullan,[†‡] James K. Li,[‡] Changchun Hao,[†] Gilbert C. Walker,[‡] and Shan Zou[†*]
[†]Steacie Institute for Molecular Sciences, National Research Council Canada, Ottawa, Ontario, Canada; and [‡]Department of Chemistry, University of Toronto, Toronto, Ontario, Canada

ABSTRACT Cholesterol is involved in endocytosis, exocytosis, and the assembly of sphingolipid/cholesterol-enriched domains, as has been demonstrated in both model membranes and living cells. In this work, we explored the influence of different cholesterol levels (5–40 mol %) on the morphology and nanomechanical stability of phase-segregated lipid bilayers consisting of dioleoylphosphatidylcholine/sphingomyelin/cholesterol (DOPC/SM/Chol) by means of atomic force microscopy (AFM) imaging and force mapping. Breakthrough forces were consistently higher in the SM/Chol-enriched liquid-ordered domains (L_o) than in the DOPC-enriched fluid-disordered phase (L_d) at a series of loading rates. We also report the activation energies (ΔE_a) for the formation of an AFM-tip-induced fracture, calculated by a model for the rupture of molecular thin films. The obtained ΔE_a values agree remarkably well with reported values for fusion-related processes using other techniques. Furthermore, we observed that within the Chol range studied, the lateral organization of bilayers can be categorized into three distinct groups. The results are rationalized by fracture nanomechanics of a ternary phospholipid/sphingolipid/cholesterol mixture using correlated AFM-based imaging and force mapping, which demonstrates the influence of a wide range of cholesterol content on the morphology and nanomechanical stability of model bilayers. This provides fundamental insights into the role of cholesterol in the formation and stability of sphingolipid/cholesterol-enriched domains, as well as in membrane fusion.

INTRODUCTION

Abundant studies on cholesterol demonstrate its importance in understanding various membrane structures and processes in cells. Cholesterol's diverse roles range from building blocks to key regulatory molecules in highly specialized membrane fusion processes such as endocytosis and exocytosis (1–5). Large variations in a number of structural and dynamical parameters of the lipid bilayer are also observed in the presence of cholesterol, illustrating its influence on the phase properties of membranes (2,3,5–10). In addition, cholesterol is closely associated with phase-segregated micro- or nanodomains in cells called rafts, which have been proposed as platforms for the preferential sorting of proteins (5,11–13). Although a recent study has demonstrated the presence of cholesterol-mediated rafts ~20 nm in size in the plasma membrane of living cells, there is nevertheless ongoing debate about their existence (11,14–19).

Several studies have investigated the effects of varying levels of cholesterol in both model and biological membranes using different techniques (3,7–9,20,21). In our previous work (22,23), we used atomic force microscopy (AFM)-based force mapping to directly correlate the self-organized structures exhibited in phase-segregated supported lipid bilayers consisting of dioleoylphosphatidylcholine/sphingomyelin/cholesterol (DOPC/SM/Chol), known to mimic rafts in cells (15,24,25), with their nanomechanical properties. We have shown quantitatively by means of the breakthrough force and elastic modulus the greater stability and degree of compactness exhibited in the Chol/SM-enriched liquid-ordered domains (L_o phase) over the DOPC-enriched fluid-disordered phase (L_d phase).

In this work, we explore how cholesterol influences the morphology, lateral organization, and mechanical stability of coexisting phases in supported DOPC/SM/Chol bilayers by AFM-based force mapping. We measure breakthrough forces in L_o and L_d phases with different Chol concentrations at a series of loading rates. In addition, we calculate the activation energies (ΔE_a) of bilayer breakthrough using the AFM tip-induced film rupture theory introduced by Butt et al. (26,27). This formalism assumes that an energy barrier must be overcome by the tip before the film ruptures; dependence of the activation energy on the force and loading rate was then obtained according to this premise. This theory is analogous to earlier theories of rupture of single molecular bonds under the influence of loading rate, relating microscopic parameters of the film with measurable quantities obtained from force measurements (28–31). Here, the activation energy is the energy required to create a hole (fracture) in the film/bilayer large enough to initiate bilayer rupture. Furthermore, two specific models for ΔE_a calculations were presented: a continuum nucleation model and a discrete molecular model (26). The former considers a thin, molecular, and homogeneous film confined between the solid substrate and the solid surface of the AFM tip. The prerequisite is that the film exhibits fluidity; it is laterally mobile with a well-defined vertical structure. In the discrete molecular model, the film is treated as having energetically favorable binding sites, formed by the substrate or surrounding molecules. When molecules move from one binding site to an

Submitted March 4, 2010, and accepted for publication April 19, 2010.

*Correspondence: Shan.Zou@nrc-cnrc.gc.ca

Editor: Peter Hinterdorfer.

0006-3495/10/07/0507/10 $2.00

doi: 10.1016/j.bpj.2010.04.044

adjacent binding site, a potential energy barrier has to be overcome. Once a critical number of molecules moves out from or reorganizes within the contact area, the large pressure on the remaining molecules triggers film rupture and tip breakthrough. In our study, we use the general formalism to calculate the rupture activation energies of DOPC/SM bilayers with 10–40% Chol. We note that the general theory we used in this study refers to neither the continuum nucleation model nor the discrete molecular model as described above, but only to the general assumption that an energy barrier must be overcome by the tip before the film ruptures. Our results demonstrate the influence of a wide range of cholesterol concentrations on the morphology and nanomechanical stability of model lipid bilayers that simulate the rafts in cells. Also, we discuss the possible implications of membrane rupture events in the presence of cholesterol in providing fundamental nanomechanical insights into other cellular processes.

MATERIALS AND METHODS

Materials

The lipids, 1,2-dioleoyl-*sn*-glycero-3-phosphocholine (DOPC, 18:1), *N*-stearoyl-D-erythro-sphingosylphosphorylcholine (SM, 18:0), and ovine wool cholesterol (Chol), were purchased from Avanti Polar Lipids (Alabaster, AL) and used as received. Texas Red 1,2-dihexadecanoyl-*sn*-glycero-3-phosphoethanolamine triethylammonium salt (TR-DHPE) was from Invitrogen Canada (Burlington, Ontario, Canada). HPLC-grade chloroform (ACP Chemicals, Montreal, Quebec, Canada), ACS-grade methanol (Fisher Scientific, Ottawa, Ontario, Canada), and Milli-Q water (Millipore, Billerica, MA), deionized to a resistivity of 18 MΩ·cm, were used in all of the experiments.

Preparation of small unilamellar vesicles

Lipid mixtures were obtained by combining the appropriate molar ratios of the different lipid components: DOPC/SM (1:1) in a series of cholesterol concentrations (5–40 mol %) with 0.3 mol % TR-DHPE, using chloroform/methanol (4:1) as solvents. The resulting solution was then exposed to a gentle stream of nitrogen and placed under vacuum overnight. The lipid film was hydrated with 18 MΩ·cm Milli-Q water to a final lipid concentration of 0.5 mg/mL before use. Small unilamellar vesicles were obtained by sonicating the lipid solution to clarity (~20–30 min) using a bath sonicator (Cole Parmer, Montreal, Quebec, Canada).

Preparation of the supported lipid bilayers

Vesicle fusion protocols for DOPC/SM/Chol lipid bilayer preparations were followed (23,32–34). Vesicle solutions of DOPC/SM/Chol containing 25 μg lipids and a final concentration of 10 mM $CaCl_2$ were deposited on freshly cleaved mica substrates (~20 μm thick) glued (Norland Optical Adhesive 88, Norland Products, Cranbury, NJ) onto glass coverslips affixed to a liquid cell. The sample was incubated at 45°C for 1 h, slowly cooled to 23°C, then extensively washed using ~150 mL 18 MΩ·cm Milli-Q water.

AFM imaging and force mapping

All AFM images were taken using the Nanowizard II BioAFM (JPK Instruments, Berlin, Germany) mounted on an Olympus 1X81 inverted confocal microscope. Silicon nitride cantilevers (DNP-S, Veeco, Santa Barbara, CA) were used in contact-mode imaging and force-mapping measurements. The spring constants, typically in the range 0.16–0.28 N/m, were determined by the thermal noise method (35) after obtaining the deflection sensitivity of the cantilever by pressing the AFM tip against a hard reference glass substrate. Cantilever deflection sensitivity measurements were performed before all force-mapping experiments. In 70% of the experiments, these measurements were also performed after the experiment. The sensitivity values before and after experiments are, within the error range, not different from each other. All AFM imaging was conducted on mica-on-glass substrates fixed to a liquid cell, and the samples were kept hydrated at all times. All AFM images were plane-fit (first-order) using the JPK Image Processing software (JPK Instruments).

In force mapping, arrays of force-distance curves were collected on bilayer samples with selected grid sizes (e.g., 64 × 64 pixels). At the center of every pixel, the scanner performed a single force spectroscopy experiment and acquired force-distance curves during approach and retraction. For DOPC/SM bilayers with 10–40% Chol, force mapping at different loading rates was performed. In our experiments, the loading rate is calculated using the deflection of the cantilever (nm) divided by the approach time. Two-dimensional visual maps of the breakthrough forces were reconstructed from 64 × 64 grids of 3 × 3-μm scan size. An applied load within the range 8–20 nN was used, unless stated otherwise.

Batch analysis of the force curves

The sets of force curves (4096 curves/set) comprising the force map were batch-analyzed using a self-developed algorithm implemented in IGOR Pro 6 (Wavemetrics, Portland, OR). For each curve, the breakthrough force was calculated, and the breakthrough force map was created using the *x*,*y* positions. The details of the analysis code are provided in the Supporting Material of our previous work (22,23).

Rupture activation energy calculation

The rupture of a lipid bilayer is considered to be an activated process wherein an energy barrier needs to be overcome by the AFM tip to form a hole or fracture in the bilayer, and it is observed as a jump or kink in a force curve (Scheme S1, *B* and *C*, in the Supporting Material) (26,27). Scheme S1 illustrates the physical events associated with different regions of typical force curves when the tip is creating an indent in a lipid bilayer. The noncontact region (Scheme S1, *O*–*A*) before the contact point (Scheme S1 *A*) indicates very little to no interaction between the tip and the bilayer, which results in a relatively constant force on the plot. As the AFM tip continues to approach and indent the bilayer, a repulsive region (Scheme S1, *A* and *B*) then follows; this region of increasing force is attributed to a combination of steric and hydration forces, as well as effective surface charges arising from the bilayer-water interface (36). At a certain force threshold, when the bilayer can no longer withstand the applied load, a sudden jump-to-contact or breakthrough occurs (Scheme S1, *B* and *C*). The magnitude of these breakthrough events is used as a measure of the bilayer's mechanical stability (22,23,26,37).

We used the theory introduced by Butt et al. to calculate the activation energy of rupture of lipid membranes (27). Details of the rupture kinetics are presented in the Supporting Material. In our experiments, the mean breakthrough force, F_0, was extracted from histograms compiled for each phase (L_d and L_o) at each loading rate. In our calculations, we used a cantilever spring constant, *k*, of ~0.25 N/m, a temperature of 296.2 K, and set the frequency at which the tip attempts to penetrate the film, *A*, equal to the cantilever's resonant frequency under water (~15 × 10^3 Hz).

RESULTS AND DISCUSSION

Bilayer morphology as a function of cholesterol concentration

AFM imaging was employed to visualize how different cholesterol compositions influence the lateral organization

of phase-separated supported lipid bilayers prepared from DOPC/SM/Chol. The AFM height images in Fig. 1 show the coexistence of the SM/Chol-enriched L_o phase (*lighter regions*) and DOPC-enriched L_d phase (*darker matrix*) in DOPC/SM/Chol with 10–40 mol % Chol. This result is in good agreement with previous studies reporting phase separation in model membranes with similar lipid mixtures (15,25,38). Specifically, extended phase separation starts to occur at 10 mol % Chol, whereas the round shape of the domains suggests the coexistence of both L_o and L_d phases. The height difference between the L_o and L_d phases is also consistent with that observed in previous studies of similar lipid mixtures: ~0.8–1.2 nm in 10–35% and ~0.6 nm in 40% Chol (18,19,23,32–34,39–42). We attribute the decrease in height difference at 40% Chol to the saturation of Chol in the L_o phase and the subsequent fluidizing effect. As a result of more Chol in the domains, SM packing is loosened, which leads to a decrease in the height of the L_o phase and, hence, a smaller height difference between the coexisting phases. This decrease at 40% Chol could also be due to the ability of Chol to thicken fluid bilayers (18,43,44). Owing to Chol saturation in the domains, some Chol may now tend to interact with the DOPC-enriched fluid phase. As a result, the thickness of the L_d phase is increased, thus decreasing the height difference between the coexisting L_o and L_d phases. This smaller height difference observed in DOPC/SM at 40% Chol closely agrees with a separate study on the same lipid mixtures in which phase-separation was observed for 50% Chol bilayers with the L_o phase ~0.4 nm taller than the L_d phase (18).

Fluorescence images of larger areas of the bilayers also show the coexistence of the L_o phase (darker domains) and L_d phase (lighter matrix) (see Fig. S1). The Texas Red dye (TR-DHPE) displays strong partitioning into the fluid-disordered phase, consequently causing the liquid-ordered domains to appear as micron-sized dark spots (34). Large dye-excluded regions (dark patch with asterisk, Fig. S1 *A*) are visible in the DOPC/SM/Chol bilayer sample with 5% Chol. This dark patch arises from the coalescence of small individual domains and bilayer defects (see Fig. S2 *A*). It is evident from both AFM and fluorescence images that the role of cholesterol is to promote phase separation into L_o and L_d phases in DOPC/SM/Chol bilayers.

Fig. 1 also demonstrates how the morphology of the DOPC/SM/Chol bilayers evolves with increasing Chol concentration. Lipid bilayers with 5–10% Chol (Fig. 1, *A* and *B*) show small domains that appear to be taller and

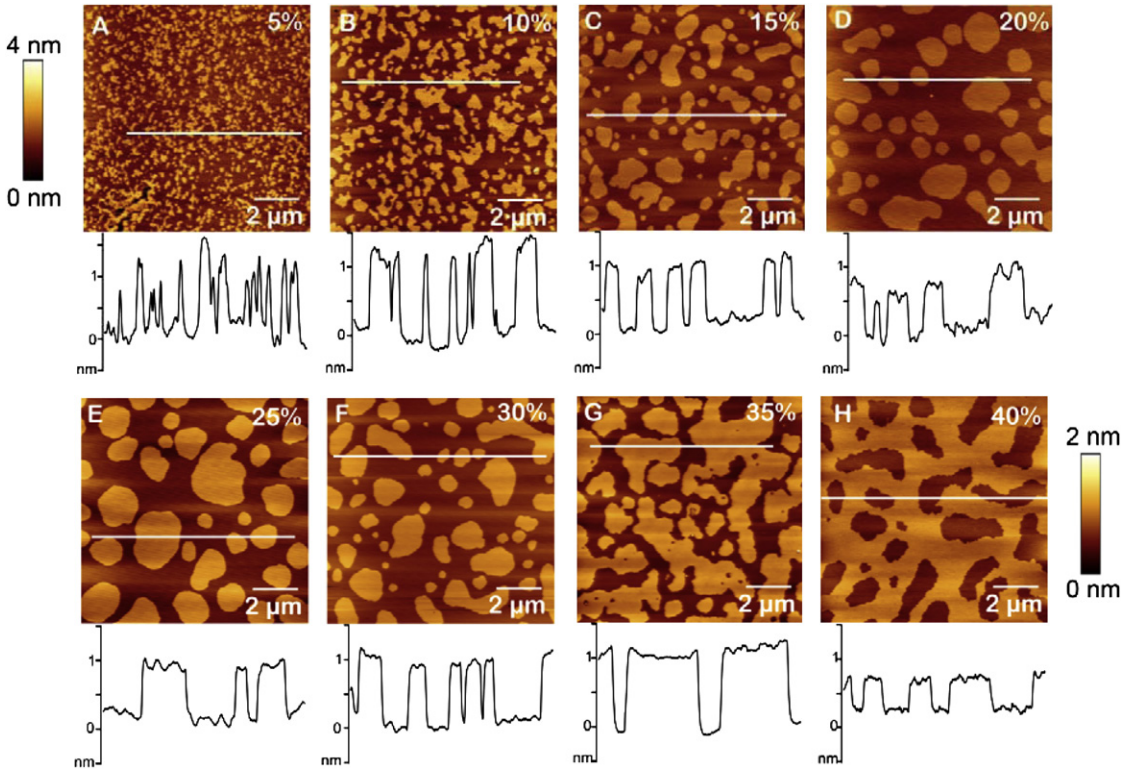

FIGURE 1 AFM height images of supported lipid bilayers. Phase separation is depicted in ternary bilayers of DOPC/SM/Chol with cholesterol content varying from 5 to 40%. (*A*) Bilayers with 5% Chol exhibit phase separation of smaller domains. (*B–G*) More distinctive phase separation between the coexisting liquid-ordered (L_o) domains and fluid-disordered (L_d) phase were observed with 10–35% Chol. (*H*) Bilayers with 40% Chol also showed distinct phase separation but with the contrast reversed compared to those observed in 10–35% Chol (the L_d phase seems to be dispersed in the L_o matrix). Cross-sectional line profiles are shown below each image. The scale bars to the left of *A* and right of *H* provide height references for the images in Fig. 1, *A–G*, and Fig. 1 *H*, respectively. All images are $10 \times 10\ \mu m^2$.

tend to form close networks with other domains. Distinctly phase-separated, round, and well-separated domains are observed with 15–30% Chol (Fig. 1, *C–F*). Elongated domains start to appear in the 30% Chol bilayer (Fig. 1 *F*), become more dominant in 35% Chol (Fig. 1 *G*), and continue to coalesce in 40% Chol (Fig. 1 *H*). This gives rise to what appears to be a phase inversion: the L_o phase now constitutes the matrix and the L_d phase assumes a more separated and rounded shape, in contrast to that of the liquid-ordered domains observed in 15–30% Chol bilayers (Fig. 1, *B–F*). In a previous study of DOPC/SM/Chol bilayers, this phase inversion, or change in percolation phase, has been observed with 30% Chol (18). It is interesting that a change in percolating and nonpercolating phases has been proposed as a trigger mechanism in the control of membrane physiology (45). The observed bilayer morphologies also suggest that three different morphological classifications exist within the range of Chol concentrations studied. In the first group (5–10% Chol), we infer that the domains of bilayers with 5% Chol are predominantly in the gel phase (see Fig. S2), whereas the domains with 10% Chol appear to be a mixture of gel and L_o phases. This inference is supported by AFM images after force mapping; the dips and holes in the line profile of the bilayer with 10% Chol indicate the existence of a gel phase (Fig. S3 *A*), in contrast to the DOPC/SM/Chol bilayer with 25% Chol, where no holes were seen, which confirms the presence of the more fluid (laterally mobile) liquid-ordered state (Fig. S3 *C*). These images after force mapping therefore indicate that the domains in 10% Chol are not solely in the L_o phase but are a mixture of both gel and L_o phases. In the second group (15–30% Chol), the domains are more rounded and separated, indicating that liquid-ordered and fluid-disordered phases coexist in the bilayer (Fig. S3 *C*). Also, with increasing Chol content in the second group, a subtle increase of the domain size is observed, confirming the known affinity of cholesterol toward sphingomyelin in the formation of SM/Chol-enriched domains (14,20,41,46). We note that the AFM image after force mapping for the bilayer with 15% Chol suggests the existence of a minimal gel-phase character in the domains (Fig. S3 *B*). In the third group (35–40% Chol), the L_o phase occupies a relatively larger area in the bilayer, further indicating the increasing interaction between the added Chol and SM. At Chol concentrations >40%, conflicting observations by different groups regarding the presence/absence of separated phases for the same lipid system presently render any hypothesis inconclusive (14,15,25,38). Phase separation was not observed on DOPC/SM/Chol giant unilamellar vesicles (GUVs) with <10% Chol (45). Our proposed classification of bilayer morphologies into three groups within the 5–40% Chol range studied is in good agreement with the fluorescence microscopy study on egg PC/brain SM/Chol, in which different regions in the phase diagrams of the coexisting liquids were observed (21,38,47).

Force mapping on the bilayers: dependence of the breakthrough force on loading rate

Although the AFM height images in Fig. 1 do not provide quantitative nanomechanical information on these bilayers, they do reveal some insight into how DOPC/SM/Chol bilayers evolve with increasing Chol concentration. To investigate how cholesterol influences the mechanical stability and lateral organization of the bilayers, we performed AFM-based force mapping on DOPC/SM/Chol bilayers with 10–40 mol % Chol while keeping DOPC and SM at a 1:1 ratio. Consistent with our previous studies, breakthrough forces were obtained in the coexisting phases—liquid-ordered domains and fluid-disordered phase—at different loading rates (26,27,37). We report our results as breakthrough force maps (Fig. 2). As noted in the Materials and Methods section, the breakthrough force is the maximum force that a bilayer withstands before it ruptures and is used as a measure of the bilayer's mechanical stability.

Representative breakthrough force maps of DOPC/SM/Chol bilayers with 15, 20, and 25% Chol at 200, 800, and 2000 nm/s loading rates, respectively, are displayed in Fig. 2, *A–I*. The correlated AFM height images and breakthrough force maps for 20% Chol in Fig. S4 clearly show that lighter regions and darker matrix in the breakthrough force maps correspond to the taller L_o and shorter L_d phase, respectively, in AFM height images. Also, the L_o and L_d phases correspond to the higher and lower mean breakthrough forces, respectively, in the correlated histograms. The mean breakthrough force peaks were obtained from Gaussian fits of the force-distribution histograms. The higher breakthrough force exhibited in the SM/Chol-enriched L_o phase reflects the more efficient packing between Chol and SM in the L_o phase in comparison to the DOPC-enriched L_d phase. Fig. 2 also reveals that mean breakthrough forces depend on the loading rate, i.e., the breakthrough force increases with increasing loading rate (26,27,37). In addition, at a fixed loading rate, the breakthrough forces tend to decrease with increased Chol concentration. Furthermore, the difference between the breakthrough forces in the two phases in the bilayer with 15% Chol is larger than between those with 20% and 25% Chol, confirming the preferential affinity of Chol to SM (14,20,41,46). At a lower Chol concentration, Chol tends to fully incorporate into the domains, resulting in more disparate breakthrough force values in the coexisting phases.

Force mapping on the bilayers: dependence of breakthrough forces on Chol concentration

To clearly illustrate how the breakthrough force varies with Chol concentration, Fig. 3 is a plot of mean breakthrough forces versus mol % Chol at 200 nm/s. The solid and open circles correspond to the L_o and L_d phases, respectively. Four main results were observed in this plot. First, in comparison to the L_d phase, higher mean breakthrough

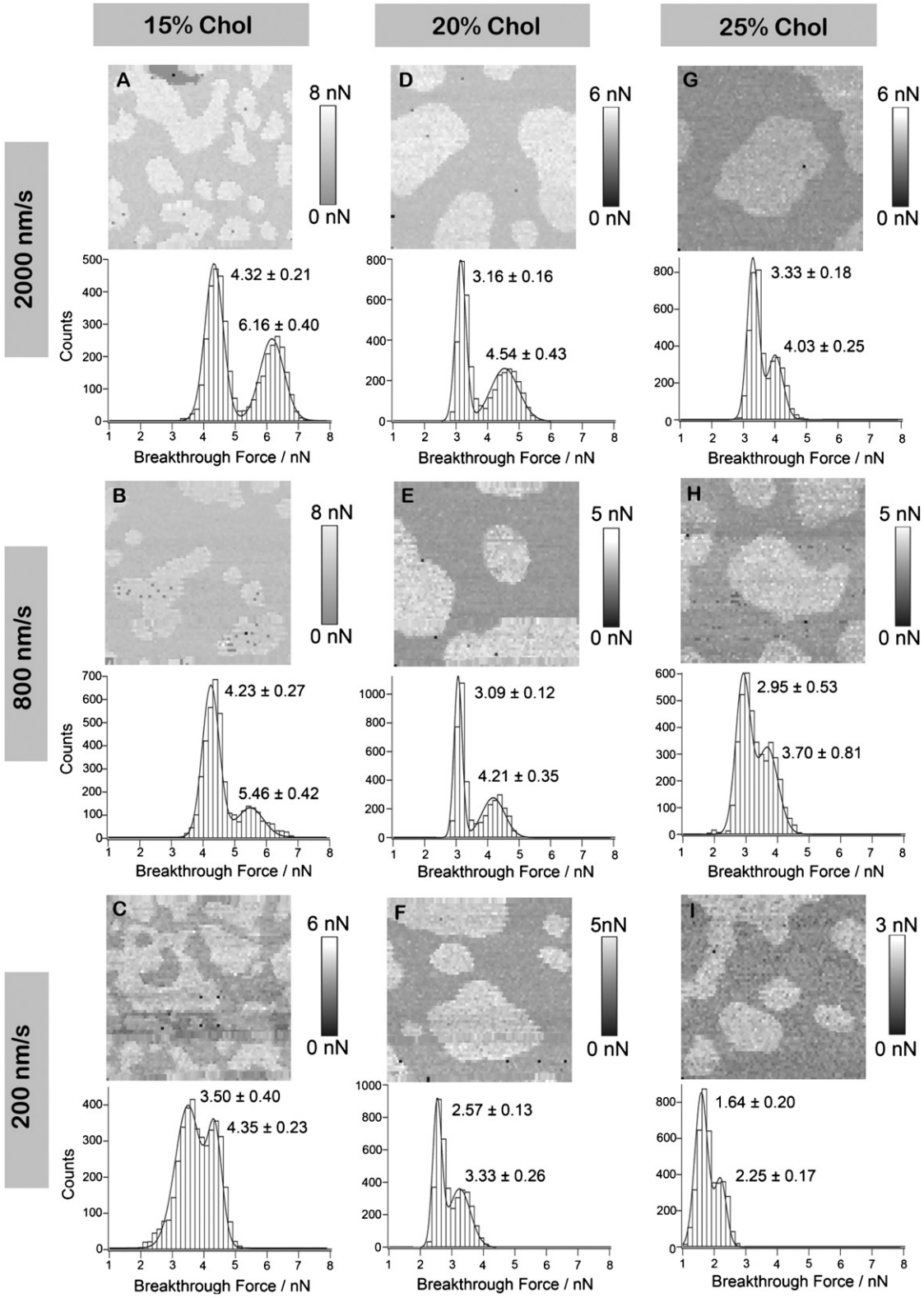

FIGURE 2 Representative breakthrough force maps and corresponding histograms of DOPC/SM/Chol bilayers at a series of loading rates. Breakthrough force maps were reconstructed from 64 × 64-pixel force-mapping experiments and the corresponding histograms on bilayers with (*A–C*) 15% Chol, (*D–F*) 20% Chol, and (*G–I*) 25% Chol at loading rates of 200 nm/s (*C*, *F*, and *I*), 800 nm/s (*B*, *E*, and *H*), and 2000 nm/s (*A*, *D*, and *G*), respectively. All histograms consist of 4096 force curves, and the numbers in the histogram represent mean ± SD breakthrough force values from Gaussian fits. The darker region in the upper left corner of *A* is a defect in the bilayer. All breakthrough force maps are 3 × 3 μm^2.

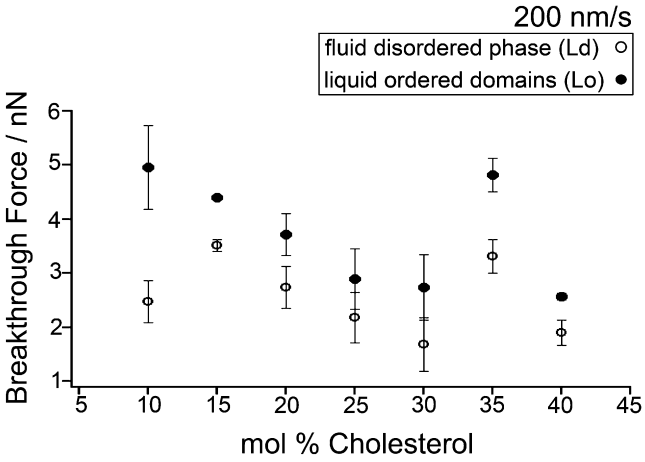

FIGURE 3 Breakthrough forces for DOPC/SM/Chol bilayers with 10–40% Chol at 200 nm/s. Error bars are the mean ± SD from a set of 2–10 force maps, each containing 4096 force curves.

forces were consistently detected in the L_o phase. This higher nanomechanical stability in the L_o phase is due to the enhanced SM-Chol interaction, which results in a more ordered lipid organization compared to the case of interactions between Chol and unsaturated phospholipids (14,20,38,41,46). The second significant result is that bilayers with 10% Chol exhibit the largest difference between the domains and L_d phases, and this is indicative of domains that maintain a partial gel-like nature (see Fig. S3 *A*). Another main finding is that for bilayers with 10–30% Chol, the breakthrough forces in both phases tend to decrease as Chol concentration increases, consistent with the fluidizing effect of Chol and its role in the formation of a liquid-ordered phase with a more relaxed lipid packing than the pure SM gel phase. This is consistent with a previous fluorescence correlation spectroscopy (FCS) study of DOPC/SM/Chol GUVs, in which an increased Chol concentration resulted in increased lipid mobility in SM-enriched domains (38). More Chol in the DOPC/SM/Chol bilayer relieves stress, and as a result, a lower force is necessary to induce rupture (i.e., the breakthrough force is lower). The fourth result of interest is the sudden increase of the breakthrough force in both the L_o and L_d phases at 35% Chol; this transition is consistent with the observed change in the bilayer morphology in Fig. 1, *F* and *G* (a shift from rounded to more elongated domains). This sudden increase could be due to the coalescence effect, i.e., individual domains start to form a network with neighboring domains, as revealed by the more elongated features in bilayers with 35% (Fig. 1 *G*). At this Chol concentration, the interaction between the constituent lipids in the coexisting phases may have led to an increase in the line tension wherein the decrease in boundary energy dominates the unfavorable entropy of merging, consequently resulting in coalescence of the domains (48). Force mapping was not performed on DOPC/SM with 5% Chol due to the domains being relatively small and not well separated.

The plot of breakthrough force versus Chol content (Fig. 3) supports the three-group classification observed in Fig. 1. It can then be presumed from Fig. 3 that DOPC/SM/Chol bilayers with 10% Chol fall in the first group, those with 15–30% Chol in the second group, and those with 35–40% Chol in the third group. These correlated results by AFM imaging and force mapping demonstrate the effective use of force mapping in studying the influence of a wide range of Chol concentrations on the nanomechanical stability and the lateral organization of coexisting phases in model bilayers with compositions that simulate those of biological membranes.

Rupture activation energy of DOPC/SM/Chol at varying Chol concentrations

As illustrated in Fig. 4, the same dependence of the breakthrough force on loading rate observed in Fig. 2 (i.e., breakthrough forces in both L_o and L_d phases increase with increasing loading rate) was observed for other cholesterol concentrations. The slope (*b*) and the *y*-intercept (*a*) obtained from linear fits to Eq. S9 were used to calculate the rupture activation energy. As noted in the Materials and Methods section, ΔE_a can be explicitly expressed as a function of force proportional to k_BT, when the mean breakthrough forces increase linearly with the logarithm of loading rates. When extrapolated to zero mean breakthrough force, the relation represented in Eq. S10 provides the activation energy of the bilayer rupture in the absence of an applied force (27).

Our values for calculated rupture activation energy, determined using Eq. S10 with $F_o = 0$, are summarized in Table S1 and plotted as a function of Chol content in Fig. 5. The solid and open squares correspond to L_o and L_d phases, respectively. Our results yield a range of activation energies that vary for L_d and L_o phases according to the Chol concentration. DOPC/SM/Chol bilayers with 10, 25, 30, and 40% Chol provided ΔE_a values in the range 75–100 kJ/mol, whereas higher ΔE_a—in the range 100–125 kJ/mol—were obtained for bilayers with 15, 20, and 35% Chol. The difference in ΔE_a values between the coexisting phases with different mol % Chol is within 10 kJ/mol, except in the case of 15 mol % Chol, where the L_d phase is 30 kJ/mol greater than the L_o phase. Our data did not show dependence in the activation energy for the different lipid phases. The absence of a clear trend or a linear correlation between ΔE_a and Chol content underlines the complex nature of the rupture process in bilayers of this ternary mixture (49). Nevertheless, when compared to the reported activation energies of membrane fusion and other cellular processes using different techniques, ΔE_a values (Table S1) obtained by force measurements are in remarkable agreement. For instance, activation energies of a lipid flip-flop in highly

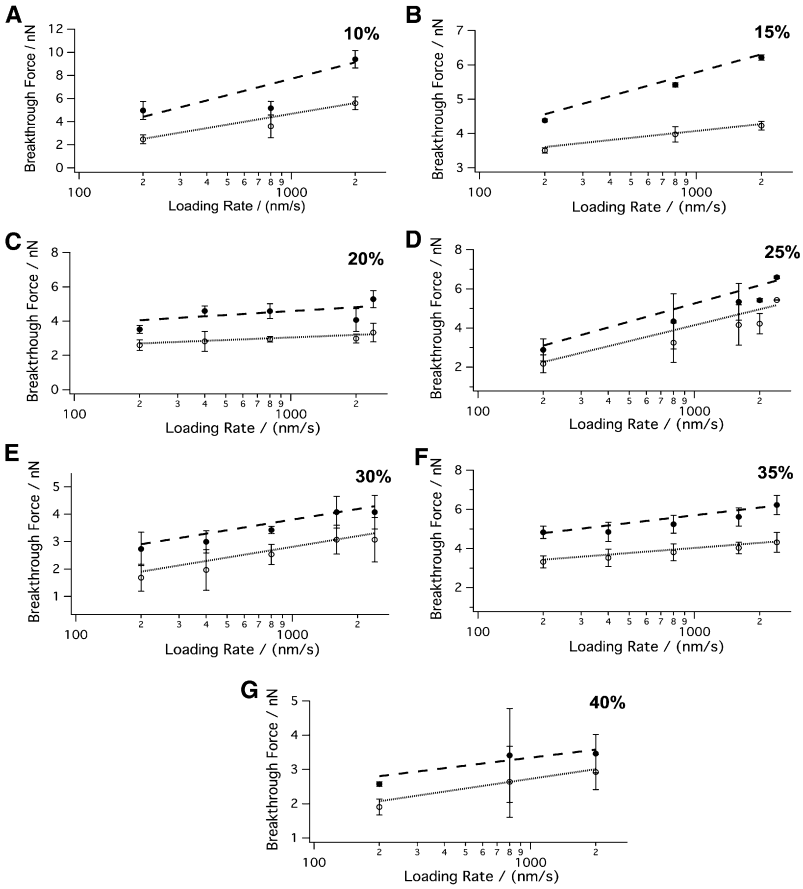

FIGURE 4 Dependence of the breakthrough force on loading rate for different cholesterol concentrations. (*A–G*) Breakthrough forces of the coexisting phases (L_o and L_d) of DOPC/SM/Chol bilayers (10–40% Chol, respectively) at different loading rates (200, 400, 800, 2000, and 2400 nm/s).

curved vesicles (50) were found to be 100 kJ/mol, and those for lipid desorption from a membrane (51) were 92 kJ/mol. In addition, pore formation during secretory granule release (52), has a ΔE_a of 96 kJ/mol, with 88 kJ/mol and 113 kJ/mol for PEG-mediated fusion of protein-free model lipid bilayers (53). As a further comparison, activation energies of 20–50 kJ/mol are obtained for the diffusion of lipid molecules in phosholipid bilayers without rafts using proton NMR measurements and fluorescence excimer techniques (54,55).

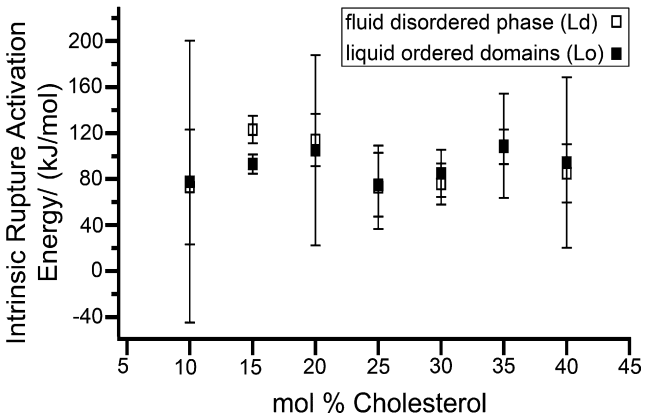

FIGURE 5 Rupture activation energies of the coexisting phases (L_o and L_d) in DOPC/SM/Chol bilayers with 10–40% cholesterol.

We also approximated the number of lipid molecules involved in the rupture process by using the activation energy values in Table S1 to represent the total free energy of hydration of a solute molecule, G_h° given by

$$\Delta G_h^\circ = \sum_i g_i A_i, \tag{1}$$

where g_i is the proportionality constant pertaining to a functional group i, which in our case was taken as an aliphatic group to represent the aliphatic tails of the lipids; and A_i is the conformation-dependent accessible surface area (56). Comparison of the A_i obtained using Eq. 1 with the cross-sectional area of a cylinder (assuming that exposed surface area of the lipid bilayer has this conformation), we obtained three to six lipid molecules. This compares well with the four to seven lipid molecules obtained for dioleoylphosphatidylserine and dioleoyloxypropyl trimethylammonium chloride using the discrete molecular model (26). Our approximation implies that the structural change at the breakthrough transition state involves this number of lipid molecules, which effectively corresponds to binding sites that are in energetically favorable positions, as described in the discrete molecular model by Butt et al. (26).

Our work draws attention to a number of important cell membrane processes involving cholesterol. The AFM tip-induced rupture of the DOPC/SM/Chol bilayers at various

Chol concentrations can serve as a model platform for studying relevant cellular processes, such as membrane fusion and poration (57–60), and can represent proteins, viruses, or other trigger particles that mediate pore formation and bilayer rupture. An example of this is the well-known fusion-inducing agent lysolecithin, which may operate by creating small defects in the bilayer (58). Indeed, the process of fusion requires a breaking of the membrane, at least during the coalescence of the fusion vesicles (58). Since cholesterol is reported to be involved in a wide range of significant cellular events, it is important to know how it influences the lateral organization and mechanical stability of lipid bilayers. Using AFM-based force mapping, we revealed that Chol content affects the morphology and mechanical stability of the DOPC/SM/Chol model membrane. Quantifying the breakthrough forces enabled us to directly correlate the nanomechanical stability with the bilayer's morphology in a wide range of Chol concentrations. This direct correlation is not apparent in conventional force measurements (e.g., nonforce-mapping experiments). Moreover, there is a significant improvement in statistics with the massive number of force curves obtained from a force map. In addition, force mapping provides a biophysical means of studying phase-segregated lipid bilayers that requires no dye label, thus avoiding the occasionally inconsistent partitioning behavior of dye molecules, which affects lipid organization (14,42,61,62).

As for the possibility that the force mapping technique mechanically alters the organization of the bilayer, AFM images obtained at the same location before and after force mapping in our previous work indicate no significant restructuring of the bilayer based on the unchanged domain sizes and relative positions (24). In addition, the possibility of tip contamination as a result of force mapping measurements has already been addressed by Leonenko et al. in their study of dipalmitoylphosphatidylcholine (DPPC) bilayers measured with loading rates in the range 0.5–2500 nm/s (36). In that study, no evidence of lipids permanently coating the AFM tip was observed. Continuous imaging of the bilayers did not show resolution degradation or changes in force curves that could arise from uncontrollable lipid coating of the AFM tip. In our study, for 50% of all tips (25 of 50) used to collect 20 images and 10 force maps, we observed no permanent contamination; on other occasions, we observed effects of contamination shown by dull breakthroughs. These gradual breakthroughs did not affect our statistics, as they were still recognized and processed by our analysis algorithm.

The distribution of the breakthrough forces in Fig. 2 demonstrates that the observed AFM-tip-induced rupture in the lipid bilayer is a statistical process depending on the probability that the AFM tip ruptures the bilayer at a certain breakthrough force (26). This probability increases with increasing breakthrough force. Given this relation between rupture probability and breakthrough force, Eq. S10 predicts that the activation energy will decrease with increasing mean breakthrough force, hence, with increasing loading rate. Since we obtained lower breakthrough forces in the L_d phase at all Chol concentrations (Figs. 3 and 4), we would have expected higher activation energies in the L_d phase than in L_o phase. This holds true with 15–20% Chol, but is not the case for other Chol concentrations. Furthermore, the tendency of the breakthrough force to decrease with increasing Chol content (Fig. 3) should also lead to higher ΔE_a values with increasing Chol content. However, there is no clear dependence of ΔE_a on mol % Chol observed in our study. This result implies the presence of a richer microscopic behavior of the bilayers in the presence of Chol, where incremental addition of Chol does not always have the same thermodynamic effect (9). Further evidence of the nonconforming trend of the effect of cholesterol level can be found in a recent study using x-ray scattering methods; it has been demonstrated that the effect of cholesterol is not universal for lipids with varying numbers of saturated chains (8).

When a wider range of loading rates is used (e.g., rates that are different by orders of magnitude), breakthrough force versus loading rate plots (Fig. 4) can be used to reveal the energy landscape of the rupture process. This has been well demonstrated in unfolding of proteins (63), receptor-ligand dissociation (64), and fusion of floating lipid bilayers (65). In the latter case, a pronounced dependence of the fusion force on the compression rate was observed for DMPC and egg PC, which has been interpreted as evidence of the presence of a single energy barrier in the fusion of the lipid bilayers.

The plot of breakthrough force versus Chol content in Fig. 3 can be compared to typical *xy* composition plots used to estimate the lipid composition of a given phase-segregated bilayer when the breakthrough force is known, which can easily be extracted from breakthrough force maps. As demonstrated in our previous work and those of others, the breakthrough force is an intrinsic property of a bilayer that is strongly dependent on the bilayer's chemical composition (23,66–68). As such, it is regarded as a fingerprint of bilayer stability analogous to the force needed to unfold a single protein (69), the force required for the transition from double-stranded to single-stranded DNA (70), and the force needed to indent single crystals (71).

CONCLUSIONS

In this study, the influence of different cholesterol content on the morphology, lateral organization, and nanomechanical stability of phase-segregated lipid bilayers with compositions that simulate cell membranes was examined. The AFM height images of DOPC/SM/Chol bilayers with 5–40% Chol demonstrate the involvement of Chol in the formation of liquid-ordered domains in phase-segregated bilayers. Force mapping on these bilayers reveals that the nanomechanical stability of the coexisting L_o and L_d phases

decreases with increasing Chol content, confirming the fluidizing effect of Chol. The observed dependence of the breakthrough force on loading rate in both phases allowed us to calculate the activation energies of bilayer rupture at zero applied force. The obtained ΔE_a values agree well with reported values for biomembrane and model membrane fusion processes. This study demonstrates the influence of cholesterol on the mechanical stability and lateral organization of model membranes, providing fundamental nanomechanical insights into the role of cholesterol in the formation and stability of SM/Chol-enriched domains, as well as in membrane fusion.

SUPPORTING MATERIAL

Details of the rupture kinetics, fluorescence images of 5-40% Chol in DOPC/SM/Chol bilayers, and AFM images after force mapping are available at http://www.biophysj.org/biophysj/supplemental/S0006-3495(10)00542-4

We thank Dr. Linda Johnston for stimulating discussions.

This work was supported by the National Research Council (NRC) of Canada Nanometrology program and the National Sciences and Engineering Research Council (NSERC) of Canada Strategic Network (BiopSys, University of Toronto Fund 486163).

REFERENCES

1. Churchward, M. A., T. Rogasevskaia, …, J. R. Coorssen. 2005. Cholesterol facilitates the native mechanism of Ca^{2+}-triggered membrane fusion. *J. Cell Sci.* 118:4833–4848.
2. Lange, Y. 1992. Tracking cell cholesterol with cholesterol oxidase. *J. Lipid Res.* 33:315–321.
3. Méléard, P., C. Gerbeaud, …, P. Bothorel. 1997. Bending elasticities of model membranes: influences of temperature and sterol content. *Biophys. J.* 72:2616–2629.
4. Rodal, S. K., G. Skretting, …, K. Sandvig. 1999. Extraction of cholesterol with methyl-β-cyclodextrin perturbs formation of clathrin-coated endocytic vesicles. *Mol. Biol. Cell.* 10:961–974.
5. Yeagle, P. L. 1985. Cholesterol and the cell-membrane. *Biochim. Biophys. Acta.* 822:267–287.
6. Henriksen, J., A. C. Rowat, and J. H. Ipsen. 2004. Vesicle fluctuation analysis of the effects of sterols on membrane bending rigidity. *Eur. Biophys. J.* 33:732–741.
7. Pal, R., Y. Barenholz, and R. R. Wagner. 1980. Effect of cholesterol concentration on organization of viral and vesicle membranes. Probed by accessibility to cholesterol oxidase. *J. Biol. Chem.* 255:5802–5806.
8. Pan, J. J., T. T. Mills, S. Tristram-Nagle, and J. F. Nagle. 2008. Cholesterol perturbs lipid bilayers nonuniversally. *Phys. Rev. Lett.* 100:198103.
9. Parasassi, T., A. M. Giusti, …, E. Gratton. 1995. Abrupt modifications of phospholipid bilayer properties at critical cholesterol concentrations. *Biophys. J.* 68:1895–1902.
10. Venegas, B., I. P. Sugár, and P. L. G. Chong. 2007. Critical factors for detection of biphasic changes in membrane properties at specific sterol mole fractions for maximal superlattice formation. *J. Phys. Chem. B.* 111:5180–5192.
11. Brown, D. A., and E. London. 1998. Functions of lipid rafts in biological membranes. *Annu. Rev. Cell Dev. Biol.* 14:111–136.
12. Pike, L. J. 2006. Rafts defined: a report on the Keystone symposium on lipid rafts and cell function. *J. Lipid Res.* 47:1597–1598.
13. Simons, K., and E. Ikonen. 1997. Functional rafts in cell membranes. *Nature.* 387:569–572.
14. Crane, J. M., and L. K. Tamm. 2004. Role of cholesterol in the formation and nature of lipid rafts in planar and spherical model membranes. *Biophys. J.* 86:2965–2979.
15. Dietrich, C., L. A. Bagatolli, …, E. Gratton. 2001. Lipid rafts reconstituted in model membranes. *Biophys. J.* 80:1417–1428.
16. Eggeling, C., C. Ringemann, …, S. W. Hell. 2009. Direct observation of the nanoscale dynamics of membrane lipids in a living cell. *Nature.* 457:1159–1162.
17. Milhiet, P. E., M. C. Giocondi, …, B. Roux. 2002. AFM detection of GPI protein insertion into DOPC/DPPC model membranes. *Single Molecule.* 3:135–140.
18. Rinia, H. A., and B. de Kruijff. 2001. Imaging domains in model membranes with atomic force microscopy. *FEBS Lett.* 504:194–199.
19. Saslowsky, D. E., J. Lawrence, …, J. M. Edwardson. 2002. Placental alkaline phosphatase is efficiently targeted to rafts in supported lipid bilayers. *J. Biol. Chem.* 277:26966–26970.
20. Slotte, J. P. 1999. Sphingomyelin-cholesterol interactions in biological and model membranes. *Chem. Phys. Lipids.* 102:13–27.
21. Veatch, S. L., and S. L. Keller. 2002. Organization in lipid membranes containing cholesterol. *Phys. Rev. Lett.* 89:268101.
22. Sullan, R. M., J. K. Li, and S. Zou. 2009. Quantification of the nanomechanical stability of ceramide-enriched domains. *Langmuir.* 25:12874–12877.
23. Sullan, R. M. A., J. K. Li, and S. Zou. 2009. Direct correlation of structures and nanomechanical properties of multicomponent lipid bilayers. *Langmuir.* 25:7471–7477.
24. Brown, D. A., and E. London. 1998. Structure and origin of ordered lipid domains in biological membranes. *J. Membr. Biol.* 164:103–114.
25. Dietrich, C., Z. N. Volovyk, …, K. Jacobson. 2001. Partitioning of Thy-1, GM1, and cross-linked phospholipid analogs into lipid rafts reconstituted in supported model membrane monolayers. *Proc. Natl. Acad. Sci. USA.* 98:10642–10647.
26. Butt, H. J., and V. Franz. 2002. Rupture of molecular thin films observed in atomic force microscopy. I. Theory. *Phys. Rev. E.* 66:031601.
27. Loi, S., G. Sun, V. Franz, and H. J. Butt. 2002. Rupture of molecular thin films observed in atomic force microscopy. II. Experiment. *Phys. Rev. E.* 66:031602.
28. Bell, G. I. 1978. Models for the specific adhesion of cells to cells. *Science.* 200:618–627.
29. Evans, E. 2001. Probing the relation between force—lifetime—and chemistry in single molecular bonds. *Annu. Rev. Biophys. Biomol. Struct.* 30:105–128.
30. Heymann, B., and H. Grubmüller. 2000. Dynamic force spectroscopy of molecular adhesion bonds. *Phys. Rev. Lett.* 84:6126–6129.
31. Tees, D., R. Waugh, and D. Hammer. 2001. A microcantilever technique was used to apply force to receptor-ligand molecules involved in leukocyte rolling on blood vessel walls. *Biophys. J.* 80:668–682.
32. Chiantia, S., N. Kahya, …, P. Schwille. 2006. Effects of ceramide on liquid-ordered domains investigated by simultaneous AFM and FCS. *Biophys. J.* 90:4500–4508.
33. Ira, and L. J. Johnston. 2006. Ceramide promotes restructuring of model raft membranes. *Langmuir.* 22:11284–11289.
34. Ira, S. Zou, …, L. Johnston. 2008. Enzymatic generation of ceramide induces membrane restructuring: correlated AFM and fluorescence imaging of supported bilayers. *J. Struct. Biol.* 168:78–89.
35. Hutter, J. L., and J. Bechhoefer. 1993. Calibration of atomic-force microscope tips. *Rev. Sci. Instrum.* 64:1868–1873.
36. Leonenko, Z. V., E. Finot, …, D. T. Cramb. 2004. Investigation of temperature-induced phase transitions in DOPC and DPPC phospholipid bilayers using temperature-controlled scanning force microscopy. *Biophys. J.* 86:3783–3793.
37. Franz, V., S. Loi, …, H. H. Butt. 2002. Tip penetration through lipid bilayers in atomic force microscopy. *Colloids Surf. B Biointerfaces.* 23:191–200.

38. Kahya, N., D. Scherfeld, …, P. Schwille. 2003. Probing lipid mobility of raft-exhibiting model membranes by fluorescence correlation spectroscopy. *J. Biol. Chem.* 278:28109–28115.

39. Chiantia, S., J. Ries, …, P. Schwille. 2006. Combined AFM and two-focus SFCS study of raft-exhibiting model membranes. *ChemPhysChem.* 7:2409–2418.

40. Lawrence, J. C., D. E. Saslowsky, …, R. M. Henderson. 2003. Real-time analysis of the effects of cholesterol on lipid raft behavior using atomic force microscopy. *Biophys. J.* 84:1827–1832.

41. Sankaram, M. B., and T. E. Thompson. 1990. Interaction of cholesterol with various glycerophospholipids and sphingomyelin. *Biochemistry.* 29:10670–10675.

42. Shaw, J. E., R. F. Epand, …, C. M. Yip. 2006. Correlated fluorescence-atomic force microscopy of membrane domains: structure of fluorescence probes determines lipid localization. *Biophys. J.* 90:2170–2178.

43. Levine, Y. K., and M. H. Wilkins. 1971. Structure of oriented lipid bilayers. *Nat. New Biol.* 230:69–72.

44. Nezil, F. A., and M. Bloom. 1992. Combined influence of cholesterol and synthetic amphiphilic peptides upon bilayer thickness in model membranes. *Biophys. J.* 61:1176–1183.

45. Vaz, W. L. C. 1994. Diffusion and chemical reactions in phase-separated membranes. *Biophys. Chem.* 50:139–145.

46. Simons, K., and E. Ikonen. 2000. How cells handle cholesterol. *Science.* 290:1721–1726.

47. Veatch, S. L., and S. L. Keller. 2005. Seeing spots: complex phase behavior in simple membranes. *Biochim. Biophys. Acta.* 1746:172–185.

48. Frolov, V. A., Y. A. Chizmadzhev, …, J. Zimmerberg. 2006. ''Entropic traps'' in the kinetics of phase separation in multicomponent membranes stabilize nanodomains. *Biophys. J.* 91:189–205.

49. Bentz, J. 1992. Intermediates and kinetics of membrane fusion. *Biophys. J.* 63:448–459.

50. De Kruijff, B., and E. J. Van Zoelen. 1978. Effect of the phase transition on the transbilayer movement of dimyristoyl phosphatidylcholine in unilamellar vesicles. *Biochim. Biophys. Acta.* 511:105–115.

51. Jones, J. D., and T. E. Thompson. 1990. Mechanism of spontaneous, concentration-dependent phospholipid transfer between bilayers. *Biochemistry.* 29:1593–1600.

52. Oberhauser, A. F., J. R. Monck, and J. M. Fernandez. 1992. Events leading to the opening and closing of the exocytotic fusion pore have markedly different temperature dependencies. Kinetic analysis of single fusion events in patch-clamped mouse mast cells. *Biophys. J.* 61:800–809.

53. Lee, J., and B. R. Lentz. 1998. Secretory and viral fusion may share mechanistic events with fusion between curved lipid bilayers. *Proc. Natl. Acad. Sci. USA.* 95:9274–9279.

54. Galla, H. J., W. Hartmann, …, E. Sackmann. 1979. On two-dimensional passive random walk in lipid bilayers and fluid pathways in biomembranes. *J. Membr. Biol.* 48:215–236.

55. Karakatsanis, P., and T. M. Bayerl. 1996. Diffusion measurements in oriented phospholipid bilayers by 1H-NMR in a static fringe field gradient. *Phys. Rev. E Stat. Phys. Plasmas Fluids Relat. Interdiscip. Topics.* 54:1785–1790.

56. Ooi, T., M. Oobatake, …, H. A. Scheraga. 1987. Accessible surface areas as a measure of the thermodynamic parameters of hydration of peptides. *Proc. Natl. Acad. Sci. USA.* 84:3086–3090.

57. Dimitrov, D. S., and R. K. Jain. 1984. Membrane stability. *Biochim. Biophys. Acta.* 779:437–468.

58. Taupin, C., M. Dvolaitzky, and C. Sauterey. 1975. Osmotic pressure induced pores in phospholipid vesicles. *Biochemistry.* 14:4771–4775.

59. Weirich, K. L., J. N. Israelachvili, and D. K. Fygenson. 2010. Bilayer edges catalyze supported lipid bilayer formation. *Biophys. J.* 98:85–92.

60. Zimmermann, U., G. Pilwat, …, R. Gilles. 1980. Electro-mechanical properties of human erythrocyte membranes: the pressure-dependence of potassium permeability. *J. Membr. Biol.* 54:103–113.

61. Schwille, P., J. Korlach, and W. W. Webb. 1999. Fluorescence correlation spectroscopy with single-molecule sensitivity on cell and model membranes. *Cytometry.* 36:176–182.

62. Yuan, C., J. Furlong, …, L. J. Johnston. 2002. The size of lipid rafts: an atomic force microscopy study of ganglioside GM1 domains in sphingomyelin/DOPC/cholesterol membranes. *Biophys. J.* 82:2526–2535.

63. Evans, E., and K. Ritchie. 1997. Dynamic strength of molecular adhesion bonds. *Biophys. J.* 72:1541–1555.

64. Merkel, R., P. Nassoy, …, E. Evans. 1999. Energy landscapes of receptor-ligand bonds explored with dynamic force spectroscopy. *Nature.* 397:50–53.

65. Abdulreda, M. H., and V. T. Moy. 2007. Atomic force microscope studies of the fusion of floating lipid bilayers. *Biophys. J.* 92: 4369–4378.

66. Künneke, S., D. Krüger, and A. Janshoff. 2004. Scrutiny of the failure of lipid membranes as a function of headgroups, chain length, and lamellarity measured by scanning force microscopy. *Biophys. J.* 86: 1545–1553.

67. Schneider, J., W. Barger, and G. U. Lee. 2003. Nanometer scale surface properties of supported lipid bilayers measured with hydrophobic and hydrophilic atomic force microscope probes. *Langmuir.* 19:1899–1907.

68. Garcia-Manyes, S., and F. Sanz. 2010. Nanomechanics of lipid bilayers by force spectroscopy with AFM: a perspective. *Biochim. Biophys. Acta.* 1798:741–749.

69. Carrion-Vazquez, M., A. F. Oberhauser, …, J. M. Fernandez. 1999. Mechanical and chemical unfolding of a single protein: a comparison. *Proc. Natl. Acad. Sci. USA.* 96:3694–3699.

70. Clausen-Schaumann, H., M. Rief, …, H. E. Gaub. 2000. Mechanical stability of single DNA molecules. *Biophys. J.* 78:1997–2007.

71. Fraxedas, J., S. Garcia-Manyes, …, F. Sanz. 2002. Nanoindentation: toward the sensing of atomic interactions. *Proc. Natl. Acad. Sci. USA.* 99:5228–5232.